

# Implementation of contact angles in the pseudopotential lattice

## Boltzmann simulations with curved boundaries

Q. Li,<sup>1,\*</sup> Y. Yu,<sup>1</sup> and Kai. H. Luo<sup>2</sup>

<sup>1</sup>*School of Energy Science and Engineering, Central South University, Changsha 410083, China*

<sup>2</sup>*Department of Mechanical Engineering, University College London, Torrington Place, London WC1E 7JE, UK*

\*Corresponding author: qingli@csu.edu.cn

### Abstract

The pseudopotential multiphase lattice Boltzmann (LB) model is a popular model in the LB community for simulating multiphase flows. When the multiphase modeling involves a solid boundary, a numerical scheme is required to simulate the contact angle at the solid boundary. In this work, we aim at investigating the implementation of contact angles in the pseudopotential LB simulations with curved boundaries. In the pseudopotential LB model, the contact angle is usually realized by employing a solid-fluid interaction or specifying a constant virtual wall density. However, it is shown that the solid-fluid interaction scheme yields very large spurious currents in the simulations involving curved boundaries, while the virtual-density scheme produces an unphysical thick mass-transfer layer near the solid boundary although it gives much smaller spurious currents. We also extend the geometric-formulation scheme in the phase-field method to the pseudopotential LB model. Nevertheless, in comparison with the solid-fluid interaction scheme and the virtual-density scheme, the geometric-formulation scheme is relatively difficult to implement for curved boundaries and cannot be directly applied to three-dimensional space. By analyzing the features of the three schemes, we propose a modified virtual-density scheme to implement contact angles in the pseudopotential LB simulations with curved boundaries, which does not suffer from a thick mass-transfer layer near the solid boundary and retains the advantages of the original virtual-density scheme, i.e., simplicity, easiness for implementation, and low spurious currents.

PACS number(s): 47.11.-j.

## I. Introduction

The lattice Boltzmann (LB) method has been developed into an efficient numerical methodology for simulating fluid flow and heat transfer in the past three decades [1-8]. Owing to its kinetic nature, the LB method has exhibited some distinct advantages over conventional numerical methods and has been widely used in modeling multiphase flows and interfacial phenomena. The existing multiphase LB models can be generally classified into four categories [1-3], i.e., the color-gradient LB model, the pseudopotential LB model, the free-energy LB model, and the phase-field LB model. Among these four categories, the pseudopotential LB model [9-11] is probably the simplest one. In this model, the intermolecular interactions are represented with an interaction force based on a density-dependent pseudopotential and the phase separation is naturally achieved by imposing a short-range attraction between different phases.

Historically, the first attempt of using the pseudopotential LB model to simulate wetting phenomena was made by Martys and Chen [12], who proposed a solid-fluid interaction scheme to describe the interaction between a fluid phase and a solid wall. Different contact angles were obtained by adjusting the interaction strength of the solid-fluid interaction. Another type of solid-fluid interactions was later developed by Raiskinmäki *et al.* [13,14]. In their scheme the pseudopotential serves as a pre-sum factor, while in the solid-fluid interaction scheme of Martys and Chen the pre-sum factor is the density. Kang *et al.* [15,16] have also formulated a solid-fluid interaction scheme for the pseudopotential LB model and investigated the displacement of immiscible droplets subject to gravitational forces in a two-dimensional channel and a three-dimensional duct. Moreover, based on the work of Martys and Chen, Colosqui *et al.* [17] have proposed a modified solid-fluid interaction scheme composed of a repulsive core and an attractive tail.

According to the mechanical equilibrium of a multiphase system in the presence of a boundary condition, Benzi *et al.* [18] derived a formula for the contact angle of the pseudopotential LB model and

presented an alternative treatment to implement wetting boundaries. They introduced a virtual wall density  $\rho_w$  to fix the pseudopotential at a solid wall. By tuning  $\rho_w$  from  $\rho_l$  (density of liquid phase) to  $\rho_g$  (density of gas phase), the contact angle in simulations can be varied from  $0^\circ$  to  $180^\circ$ . A similar scheme can also be found in the color-gradient multiphase LB model [19], which is called the fictitious-density scheme [20]. However, as shown in Ref. [20], the fictitious-density scheme leads to an unphysical thick mass-transfer layer near the solid boundary. Such a phenomenon can also be observed in the pseudopotential LB simulations using the virtual-density scheme [21].

Besides the aforementioned studies, Huang *et al.* [22] have investigated the wetting boundaries in the pseudopotential multi-component LB simulations and proposed a formula to determine the adhesion parameters of different components from the contact angle. In addition, the geometric-formulation scheme, which is proposed by Ding and Spelt [23] for the phase-field method, has also been employed to implement contact angles in the pseudopotential LB simulations involving flat surfaces [24,25]. Compared with the solid-fluid interaction scheme, the geometric-formulation scheme usually yields much smaller spurious currents. Moreover, it can give a slope of the liquid-gas interface that is consistent with the prescribed value of the contact angle. However, such a scheme is mainly applicable to flat surfaces and its implementation for curved boundaries is much more complicated [26] than that of the solid-fluid interaction scheme or the virtual-density scheme.

In the present work, we aim at investigating the implementation of contact angles in the pseudopotential LB simulations with curved boundaries. A modified virtual-density scheme is proposed, which retains the basic mechanism of the virtual-density scheme but does not suffer from a thick mass-transfer layer near the solid boundary. Meanwhile, it yields much smaller spurious currents than the solid-fluid interaction scheme and is easy to implement in both two-dimensional and three-dimensional space in comparison with the geometric-formulation scheme. The rest of the present paper is organized as follows. The pseudopotential multiphase LB model and the solid-fluid interaction

scheme as well as the virtual-density scheme are briefly introduced in Sec. II. The modified virtual-density scheme is proposed in Sec. III. In addition, a curved geometric-formulation scheme, which is extended from a recently developed contact angle scheme for two-dimensional phase-field simulations with curved boundaries, is also presented there. Numerical results and discussion are given in Sec. IV. Finally, a brief summary is provided in Sec. V.

## II. The pseudopotential multiphase LB model

### A. Basic formulations

The LB equation that uses a multiple-relaxation-time (MRT) collision operator can be written as follows [3,27,28]:

$$f_\alpha(\mathbf{x} + \mathbf{e}_\alpha \delta_t, t + \delta_t) = f_\alpha(\mathbf{x}, t) - \bar{\Lambda}_{\alpha\beta} (f_\beta - f_\beta^{eq}) \Big|_{(\mathbf{x}, t)} + \delta_t (G_\alpha - 0.5 \bar{\Lambda}_{\alpha\beta} G_\beta) \Big|_{(\mathbf{x}, t)}, \quad (1)$$

where  $f_\alpha$  is the density distribution function,  $f_\alpha^{eq}$  is the equilibrium distribution function,  $\mathbf{x}$  is the spatial position,  $\mathbf{e}_\alpha$  is the discrete velocity along the  $\alpha$ th direction,  $\delta_t$  is the time step,  $G_\alpha$  is a forcing term in the discrete velocity space, and  $\bar{\Lambda}_{\alpha\beta} = (\mathbf{M}^{-1} \Lambda \mathbf{M})_{\alpha\beta}$  is the collision operator, in which  $\mathbf{M}$  is a transformation matrix and  $\Lambda$  is a diagonal matrix [29-31].

Through the transformation matrix  $\mathbf{M}$ , the density distribution function  $f_\alpha$  and its equilibrium distribution  $f_\alpha^{eq}$  can be projected onto the moment space via  $\mathbf{m} = \mathbf{M}\mathbf{f}$  and  $\mathbf{m}^{eq} = \mathbf{M}\mathbf{f}^{eq}$ , respectively. Accordingly, the right-hand side of the LB equation can be rewritten as

$$\mathbf{m}^* = \mathbf{m} - \Lambda(\mathbf{m} - \mathbf{m}^{eq}) + \delta_t \left( \mathbf{I} - \frac{\Lambda}{2} \right) \mathbf{S}, \quad (2)$$

where  $\mathbf{I}$  is the unit tensor and  $\mathbf{S} = \mathbf{M}\mathbf{G}$  is the forcing term in the moment space [3,28,32,33]. Then the streaming step of the LB equation is given by

$$f_\alpha(\mathbf{x} + \mathbf{e}_\alpha \delta_t, t + \delta_t) = f_\alpha^*(\mathbf{x}, t), \quad (3)$$

where  $\mathbf{f}^* = \mathbf{M}^{-1} \mathbf{m}^*$ . The macroscopic density and velocity are determined by

$$\rho = \sum_{\alpha} f_{\alpha}, \quad \rho \mathbf{v} = \sum_{\alpha} \mathbf{e}_{\alpha} f_{\alpha} + \frac{\delta_t}{2} \mathbf{F}, \quad (4)$$

where  $\mathbf{F}$  is the total force acting on the system.

For single-component multiphase flows, the intermolecular interaction force is given by [9-11]

$$\mathbf{F}_m = -G\psi(\mathbf{x}) \sum_{\alpha} w_{\alpha} \psi(\mathbf{x} + \mathbf{e}_{\alpha} \delta_t) \mathbf{e}_{\alpha}, \quad (5)$$

where  $\psi(\mathbf{x})$  is the pseudopotential,  $G$  is the interaction strength, and  $w_{\alpha}$  are the weights. For the nearest-neighbor interactions on the D2Q9 lattice, the weights are given by  $w_{\alpha} = 1/3$  for  $|\mathbf{e}_{\alpha}|^2 = 1$  and  $w_{\alpha} = 1/12$  for  $|\mathbf{e}_{\alpha}|^2 = 2$ . The pseudopotential is taken as [34-36]

$$\psi(\mathbf{x}) = \sqrt{\frac{2(p_{EOS} - \rho c_s^2)}{Gc^2}}, \quad (6)$$

where  $p_{EOS}$  is the non-ideal equation of state and  $c_s = c/\sqrt{3}$  is the lattice sound speed, in which  $c = 1$  is the lattice constant. For such a choice, the interaction strength  $G$  is employed to ensure that the whole term inside the square root is positive.

With the type of pseudopotentials given by Eq. (6), the pseudopotential LB model usually suffers from the problem of thermodynamic inconsistency, i.e., the coexisting liquid and gas densities given by the pseudopotential LB model are inconsistent with the results given by the Maxwell construction [35-37]. To solve this problem, Li *et al.* [28,36] proposed that the thermodynamic consistency of the pseudopotential LB model can be achieved by adjusting the mechanical stability condition of the model through an improved forcing scheme. For the D2Q9 lattice model, an improved forcing scheme for the forcing term  $\mathbf{S}$  in Eq. (2) can be found in Ref. [28]. For three-dimensional models (e.g., the D3Q15 and D3Q19 lattice models), readers are referred to Refs. [32,33,38].

## B. Solid-fluid interaction scheme and virtual-density scheme

The intermolecular interaction force defined by Eq. (5) represents the cohesive force of a system. When a solid wall is encountered, an adhesive force should also be considered [22]. In order to describe

the interaction between a fluid and a solid wall, Martys and Chen [12] proposed the following solid-fluid interaction to mimic the adhesive force in the pseudopotential LB model:

$$\mathbf{F}_{\text{ads}} = -G_w \rho(\mathbf{x}) \sum_{\alpha} w_{\alpha} s(\mathbf{x} + \mathbf{e}_{\alpha} \delta_t) \mathbf{e}_{\alpha}, \quad (7)$$

where  $G_w$  is the adhesive parameter and  $s(\mathbf{x} + \mathbf{e}_{\alpha} \delta_t)$  is a switch function, which is equal to 1 or 0 for the solid or fluid phase, respectively. By adjusting the value of  $G_w$ , different contact angles can be realized. Besides Eq. (7), some other types of solid-fluid interactions can be found in Ref. [39].

The treatment or scheme that uses a virtual density was developed by Benzi *et al.* [18], who introduced a constant virtual density  $\rho_w$  to fix the pseudopotential of the solid phase, i.e.,  $\psi(\rho_w)$ . Then Eq. (5) can also be applied to the interaction between the fluid phase and the solid phase. Similarly, different contact angles can be obtained by tuning the value of  $\rho_w$ . When  $\rho_w$  varies from  $\rho_l$  to  $\rho_g$ , the contact angle varies from 0 to  $180^\circ$  [21]. The advantages of the constant virtual-density scheme lie in its simplicity and easiness for implementation, but some previous studies showed that such a scheme usually produces an unphysical mass-transfer layer near the solid boundary [7,21].

### III. Alternative contact angle schemes

#### A. Curved geometric-formulation scheme

In 2007, Ding and Spelt [23] proposed a geometric-formulation scheme to implement wetting boundaries in the phase-field method. For a two-dimensional flat surface, the geometric-formulation scheme is given by

$$C_{i,0} = C_{i,2} + \tan\left(\frac{\pi}{2} - \theta_a\right) |C_{i+1,1} - C_{i-1,1}|, \quad (8)$$

where  $C$  is the order parameter of the phase-field method,  $\theta_a$  is an analytically prescribed contact angle, and  $C_{i,0}$  is the order parameter at the ghost layer  $(i, 0)$  beneath the flat surface, in which the first index denotes the coordinate along the flat surface and the second index denotes the coordinate normal to the flat surface. Ding and Spelt [23] showed that the geometric-formulation scheme can give a

slope of the liquid-gas interface that is consistent with the prescribed value of the contact angle.

However, Eq. (8) is only applicable to flat surfaces [24,25]. Recently, Liu and Ding [26] devised a geometric-formulation scheme for two-dimensional phase-field simulations with curved surfaces, which was also referred to as “the characteristic moving contact-line model”. They considered a ghost contact-line region inside the solid phase, as illustrated in Fig. 1, where the point  $P$  is within the ghost contact-line region and  $\mathbf{n}_s$  is the unit normal vector of the solid surface. The liquid-gas interface is supposed to intersect the solid substrate along certain straight lines (or characteristics), and  $l_1$  and  $l_2$  in Fig. 1 are two possible characteristic lines of the point  $P$ , which are symmetric about  $\mathbf{n}_s$  and intersect the mesh lines at the points  $D_1$  and  $D_2$ , respectively. The order parameter at the point  $P$  is determined as follows [26]:

$$C_p = \begin{cases} \max(C_{D_1}, C_{D_2}), & \theta \leq \pi/2 \\ \min(C_{D_1}, C_{D_2}), & \theta > \pi/2 \end{cases}, \quad (9)$$

where  $C_{D_1}$  and  $C_{D_2}$  are the order parameters at the points  $D_1$  and  $D_2$ , respectively.

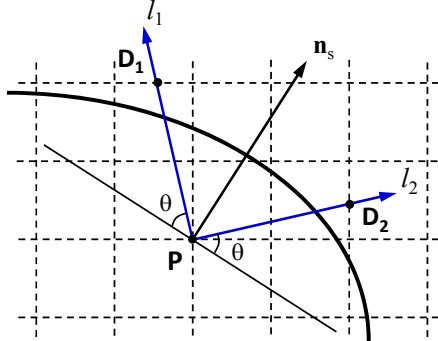


**FIG. 1.** Sketch of the characteristic lines of a point in the ghost contact-line region.

The aforementioned geometric-formulation scheme can be extended to the pseudopotential LB model. Firstly, the order parameter in Eq. (9) is replaced by the density  $\rho$ , i.e.,

$$\rho_p = \begin{cases} \max(\rho_{D_1}, \rho_{D_2}), & \theta \leq \pi/2 \\ \min(\rho_{D_1}, \rho_{D_2}), & \theta > \pi/2 \end{cases}. \quad (10)$$

In the phase-field method, the unit normal vector of the solid surface is calculated by [26]

$$\mathbf{n}_s = -\frac{\nabla C_s}{|\nabla C_s|}, \quad (11)$$

where  $C_s$  is the order parameter of the solid phase [26]. Since there is no such a quantity in the pseudopotential LB model,  $\mathbf{n}_s$  is evaluated as follows:

$$\mathbf{n}_s(\mathbf{x}) = -\frac{\sum_{\alpha} \omega_{\alpha} s(\mathbf{x} + \mathbf{e}_{\alpha} \delta_t) \mathbf{e}_{\alpha}}{\left| \sum_{\alpha} \omega_{\alpha} s(\mathbf{x} + \mathbf{e}_{\alpha} \delta_t) \mathbf{e}_{\alpha} \right|}, \quad (12)$$

where the switch function  $s(\mathbf{x} + \mathbf{e}_{\alpha} \delta_t)$  is the same as that in Eq. (7). To improve the numerical accuracy, a high-order isotropic discretization scheme can be used to evaluate  $\mathbf{n}_s$ , such as the 8th-order isotropic scheme proposed by Sbragaglia *et al.* [37,40].

When  $\mathbf{n}_s$  is determined, the unit vectors along the characteristic lines  $l_1$  and  $l_2$  can be obtained by the following vector rotation:

$$\begin{cases} \mathbf{n}_1 = (n_{s,x} \cos \theta' - n_{s,y} \sin \theta', n_{s,x} \sin \theta' + n_{s,y} \cos \theta') \\ \mathbf{n}_2 = (n_{s,x} \cos \theta' + n_{s,y} \sin \theta', -n_{s,x} \sin \theta' + n_{s,y} \cos \theta') \end{cases}, \quad (13)$$

where  $\theta' = \pi/2 - \theta$ . According to the unit vectors  $\mathbf{n}_1$  and  $\mathbf{n}_2$ , the intersection points  $D_1$  and  $D_2$  can be identified. Usually, different cases will be encountered when varying the contact angle. Figure 2 gives an example of the intersection point  $D_2$  when the contact angle  $\theta$  in Fig. 1 is changed. Obviously, the implementation of the geometric-formulation scheme is much more complex than that of the solid-fluid interaction scheme or the virtual-density scheme.

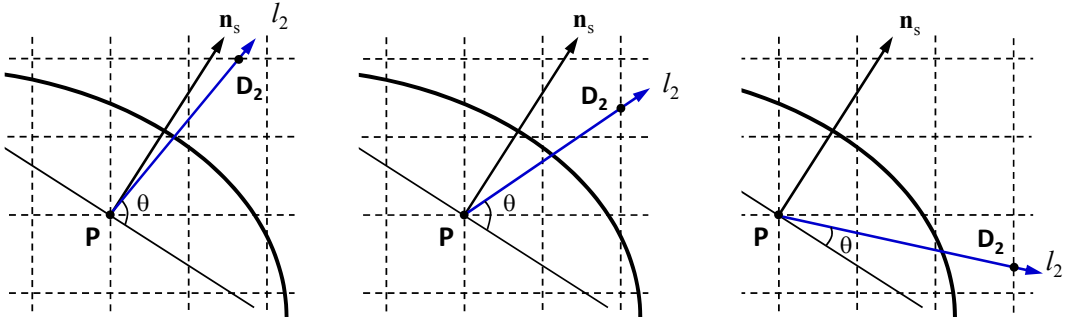


**FIG. 2.** Illustration of the intersection point  $D_2$  when the contact angle changes.

After identifying the intersection points  $D_1$  and  $D_2$ , the densities at these two points can be obtained by an interpolation of the densities at their neighboring lattice points. A quadric interpolation was used in the study of Liu and Ding [26], which involves three neighboring points around  $D_1$  or  $D_2$ . Without loss of generality, one can also employ a linear interpolation. With the densities of the points  $D_1$  and  $D_2$ , the density at the point  $P$  can be determined by Eq. (10), and then the pseudopotential can be calculated by Eq. (6). Similar to the virtual-density scheme, the curved geometric-formulation scheme also applies Eq. (5) to the interaction between the fluid phase and the solid phase.

## B. Modified virtual-density scheme

The advantage of the geometric-formulation scheme lies in that it is able to make the liquid-gas interface to intersect a solid boundary at an angle in consistence with the prescribed contact angle. On the contrary, when employing the solid-fluid interaction scheme or the virtual-density scheme, we should adjust the value of  $G_w$  or  $\rho_w$  in simulations so as to achieve a required contact angle. However, as can be seen in the previous section, the implementation of the geometric-formulation scheme is very complicated in comparison with the solid-fluid interaction and virtual-density schemes. Moreover, the above curved geometric-formulation scheme cannot be directly applied to three-dimensional space due to the fact that in two-dimensional space there are only two possible characteristic lines making an angle  $\theta$  with  $\mathbf{n}_s$  (as shown in Fig. 1), but in three-dimensional space the characteristic lines that make an angle  $\theta$  with  $\mathbf{n}_s$  form a circular cone surface around  $\mathbf{n}_s$  [20]. Hence in this section we devise an alternative contact angle scheme for the pseudopotential LB model, which is easy to implement in both two-dimensional and three-dimensional space.

Actually, in the geometric-formulation scheme the density at a solid point is also a virtual density, but the virtual density in the solid phase is a local quantity rather than a constant for the whole solid domain, which implies that the drawback of the original virtual-density scheme may be overcome when

a local virtual density is employed. On the basis of such a consideration, we propose the following formula for the virtual density in the solid phase near the curved boundary:

$$\rho_w(\mathbf{x}) = \begin{cases} \varphi \rho_{ave}(\mathbf{x}), & \varphi \geq 1, \text{ for decreasing } \theta, \\ \rho_{ave}(\mathbf{x}) - \Delta\rho, & \Delta\rho \geq 0, \text{ for increasing } \theta, \end{cases} \quad (14)$$

where  $\varphi$  and  $\Delta\rho$  are constants. When  $\varphi = 1$  or  $\Delta\rho = 0$ , Eq. (14) reduces to the standard case, i.e.,

$\rho_w(\mathbf{x}) = \rho_{ave}(\mathbf{x})$ , in which  $\rho_{ave}(\mathbf{x})$  is given by

$$\rho_{ave}(\mathbf{x}) = \frac{\sum_{\alpha} w_{\alpha} \rho(\mathbf{x} + \mathbf{e}_{\alpha} \delta_t) s_w(\mathbf{x} + \mathbf{e}_{\alpha} \delta_t)}{\sum_{\alpha} w_{\alpha} s_w(\mathbf{x} + \mathbf{e}_{\alpha} \delta_t)}, \quad (15)$$

where  $s_w(\mathbf{x} + \mathbf{e}_{\alpha} \delta_t)$  equals 1 for the fluid phase and is zero for the solid phase. The weights  $w_{\alpha}$  in Eq. (15) are the same as those in Eq. (5). For the standard case ( $\varphi = 1$  or  $\Delta\rho = 0$ ), the contact angle obtained in simulations is usually around  $\theta \approx 90^\circ$ . Accordingly, different contact angles can be realized by tuning the constant  $\varphi$  or  $\Delta\rho$ . In applications, a limiter should be applied to Eq. (14) as the local virtual density should be bounded within  $\rho_g \leq \rho_w(\mathbf{x}) \leq \rho_l$ . Hence the virtual density is set to  $\rho_l$  when  $\rho_w(\mathbf{x})$  calculated by Eq. (14) is larger than  $\rho_l$ , and is taken as  $\rho_g$  when it is smaller than  $\rho_g$ .

We now explain why we choose  $\varphi \rho_{ave}(\mathbf{x})$  rather than  $\rho_{ave}(\mathbf{x}) + \Delta\rho$  to increase the local virtual density (i.e., to decrease the contact angle  $\theta$ ) by taking a system with  $\rho_g = 0.5$  and  $\rho_l = 10$  as an example. For a solid point near the three-phase contact line with  $\rho_{ave}(\mathbf{x}) = 5$ , we can set  $\varphi = 1.1$  or  $\Delta\rho = 0.5$  to increase the virtual density of the point from 5 to 5.5. Obviously, using these two treatments, the maximum virtual densities are the same since the local virtual density  $\rho_w$  is set to  $\rho_l$  when  $\rho_w(\mathbf{x})$  calculated by Eq. (14) is larger than  $\rho_l$ . However, the minimum virtual densities are different, which are given by  $\rho_{w, \min} = 0.55$  and 1.0, respectively. It can be found that there is a relatively large gap between  $\rho_{w, \min}$  and  $\rho_g$  when using the treatment  $\rho_{ave}(\mathbf{x}) + \Delta\rho$ . Hence we adopt the treatment  $\varphi \rho_{ave}(\mathbf{x})$  for decreasing  $\theta$ . Similarly, we choose  $\rho_{ave}(\mathbf{x}) - \Delta\rho$  rather than  $\rho_{ave}(\mathbf{x})/\varphi$  for increasing  $\theta$  with the gap between  $\rho_{w, \max}$  and  $\rho_l$  being minimized.

Compared with the geometric-formulation scheme, which provides a relatively accurate solution for the virtual density in the solid phase, the present modified virtual-density scheme can be regarded as a compromised solution. However, it retains the simplicity of the original virtual-density scheme, avoids the complex implementation of the geometric-formulation scheme, and is easy to implement in both two-dimensional and three-dimensional space. Moreover, the modified virtual-density scheme can overcome the drawback of the original virtual-density scheme.

#### IV. Numerical results and discussion

In this section, numerical simulations are carried out to validate the capability of the proposed modified virtual-density scheme for implementing contact angles in the pseudopotential LB modeling with curved boundaries. Firstly, we consider the test of static contact angles on a cylindrical surface. In our simulations, the Peng-Robinson equation of state [34,41] is adopted and the saturation temperature is set to  $T_0 = 0.86T_c$ , which corresponds to a two-phase system with  $\rho_g \approx 0.38$  and  $\rho_l \approx 6.5$ . The computational domain is divided into  $N_x \times N_y = 300 \times 350$  lattices. A circular cylinder of radius  $R = 70$  is located at (150, 130) and a droplet of  $r = 50$  is initially placed on the circular cylinder with its center at (150, 230). The periodic boundary condition is applied in the  $x$  and  $y$  directions and the halfway bounce-back scheme is used to treat the curved solid boundary. The kinematic viscosity is taken as  $\nu = 0.15$  for both the liquid and gas phases.

The static contact angles obtained by the virtual-density scheme, the modified virtual-density scheme, the solid-fluid interaction scheme, and the geometric-formulation scheme are shown in Figs. 3, 4, 5, and 6, respectively. From the figures we can see that all of the schemes are capable of modeling different contact angles on the cylindrical surface through adjusting the constant or parameter in the schemes. However, Fig. 3 clearly shows that the virtual-density scheme causes a thick mass-transfer layer near the solid boundary. On the contrary, there is no such an unphysical mass-transfer layer in the

results of the modified virtual-density scheme, as shown in Fig. 4. Since the difference between the original and modified virtual-density schemes just lies in that a constant virtual density is used in the original scheme while a local virtual density is employed in the modified scheme, it can be deduced that the unphysical thick mass-transfer layer in Fig. 3 is attributed to the constant virtual density in the original scheme.

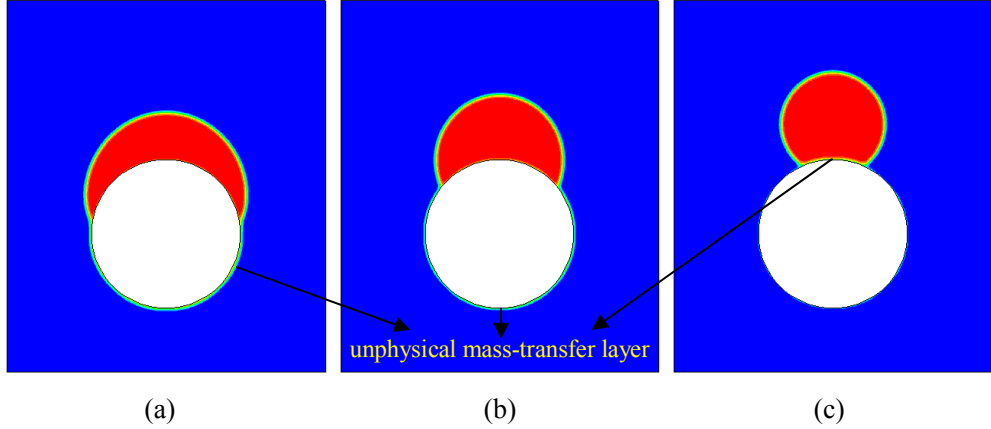


**FIG. 3.** Static contact angles obtained by the virtual-density scheme. (a)  $\rho_w = 4.5$ , (b)  $\rho_w = 3.25$ , and (c)  $\rho_w = 1.5$ . From left to right  $\theta \approx 31^\circ, 65^\circ$ , and  $121^\circ$ , respectively.

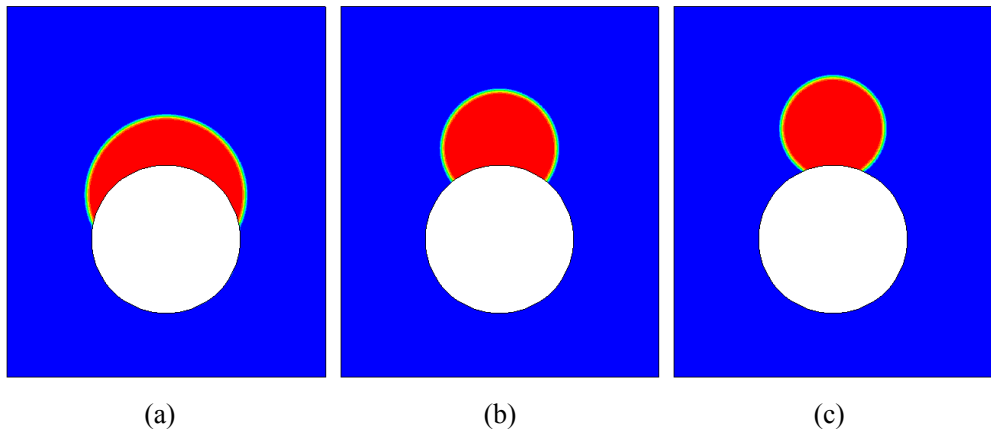


**FIG. 4.** Static contact angles obtained by the modified virtual-density scheme. (a)  $\varphi = 1.4$ , (b)  $\varphi = 1$ , and (c)  $\Delta\rho = 0.5$ . From left to right  $\theta \approx 34^\circ, 88^\circ$ , and  $125^\circ$ , respectively.

Furthermore, from Fig. 5(c) we can also observe a mass-transfer layer in the case of  $G_w = 1.2$  when using the solid-fluid interaction scheme. Actually, the adhesive force defined by Eq. (7) is a local quantity. However, when the two three-phase contact lines are very close, the locality of the adhesive

force will be affected, which is probably the reason why a mass-transfer layer appears in Fig. 5(c) rather than in Fig. 5(a) or Fig. 5(b). The results of the geometric-formulation scheme are presented in Fig. 6. Some slight deviations can be observed between the numerically obtained contact angles and the analytically prescribed contact angles given in Eq. (13), which may arise from the use of a linear interpolation in the present simulations.

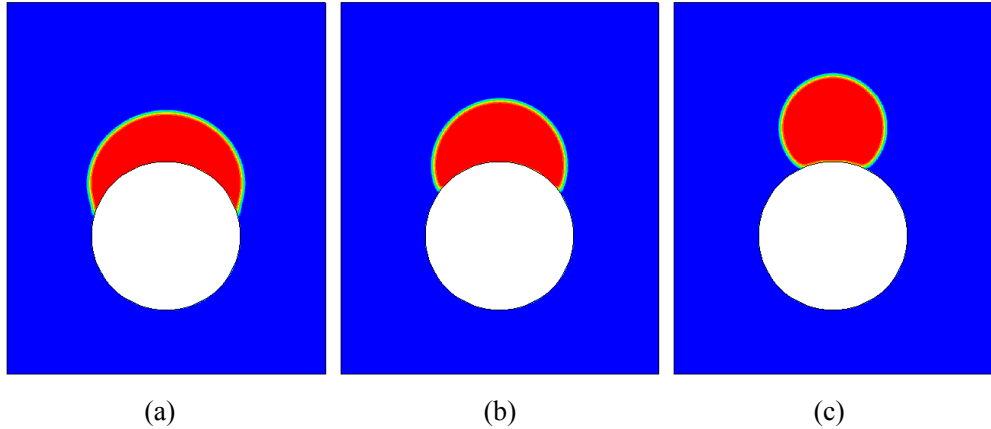


**FIG. 5.** Static contact angles obtained by the solid-fluid interaction scheme. (a)  $G_w = -0.6$ , (b)  $G_w = 0.3$ , and (c)  $G_w = 1.2$ . From left to right  $\theta \approx 38^\circ$ ,  $59^\circ$ , and  $119^\circ$ , respectively.

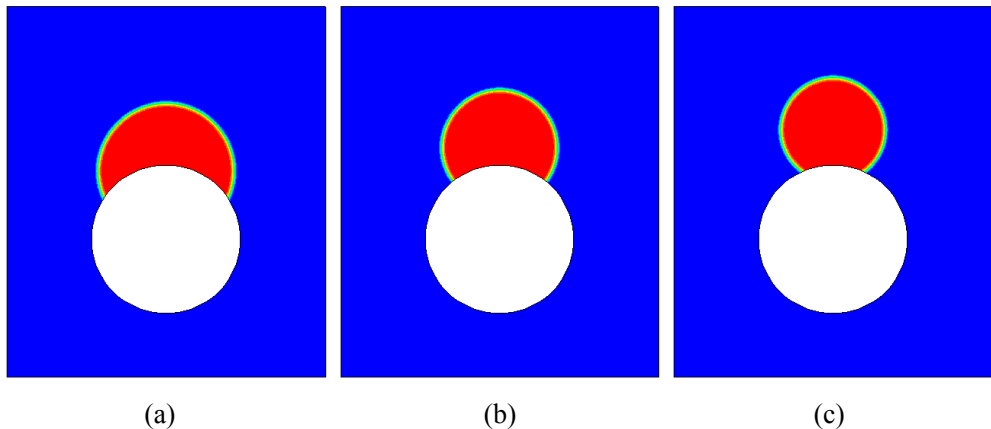


**FIG. 6.** Static contact angles obtained by the geometric-formulation scheme. (a)  $\theta_a = 60^\circ$ , (b)  $\theta_a = 90^\circ$ , and (c)  $\theta_a = 120^\circ$ . From left to right  $\theta \approx 58^\circ$ ,  $88^\circ$ , and  $121^\circ$ , respectively.

Figure 7 compares the spurious currents produced by the solid-fluid interaction scheme at  $G_w = 1.2$  and the virtual-density scheme at  $\rho_w = 1.5$ . From the figure we can see that the spurious currents caused by the solid-fluid interaction scheme are much larger than those produced by the

virtual-density scheme. To quantify the numerical results, a comparison of the maximum spurious currents caused by the four schemes is made in Fig. 8, from which we can find that the maximum spurious currents are in the order of 0.1 (lattice unit) for the solid-fluid interaction scheme but are smaller than 0.006 for the other schemes. As previously mentioned, in the geometric-formulation scheme the density within the solid phase is also a virtual density. Hence the results in Fig. 8 indicate that applying the intermolecular interaction force Eq. (5) to the interaction between a fluid phase and a solid phase with a virtual density is better than using a solid-fluid interaction force in terms of reducing the spurious currents. Moreover, Fig. 8 also shows that the maximum spurious currents yielded by the virtual-density scheme are larger than those given by the geometric-formulation scheme and the modified virtual-density scheme, which means that the spurious currents can be further reduced when employing a local virtual density to replace a constant virtual density.

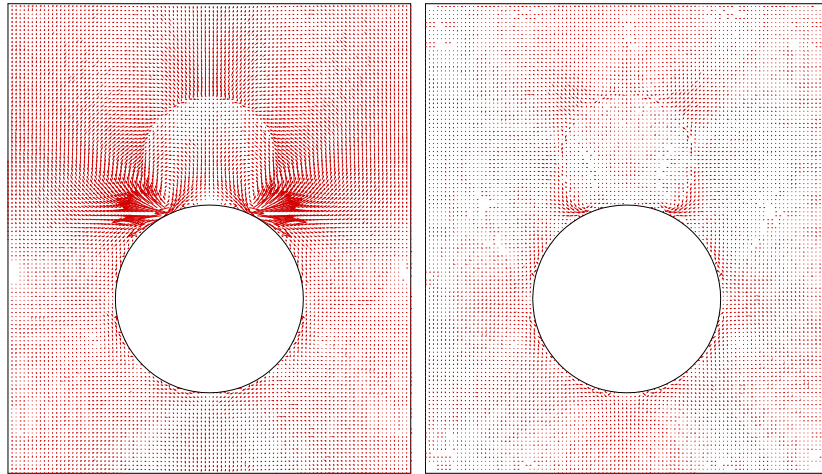


**FIG. 7.** The spurious currents produced by (left) the solid-fluid interaction scheme at  $G_w = 1.2$  and (right) the virtual-density scheme at  $\rho_w = 1.5$ .

The influence of the spurious currents has been well studied in the literature and in the present work we mainly reveal the adverse effects of the unphysical mass-transfer layer near the solid boundary through the test of droplet impact on a cylindrical surface. The computational domain is now chosen as  $N_x \times N_y = 300 \times 400$ . The circular cylinder with  $R = 70$  is located at (150, 180) and the droplet of

$r = 50$  is initially placed at  $(150, 310)$ . The initial velocity of the droplet is taken as  $\mathbf{u} = (0, -U_0)$  with  $U_0 = 0.06$  and the Reynolds number  $\text{Re} = U_0(2r)/\nu$  is set to 600. In this test, the static contact angle on the cylindrical surface is tuned to be  $\theta \approx 60^\circ$  for all the investigated schemes.

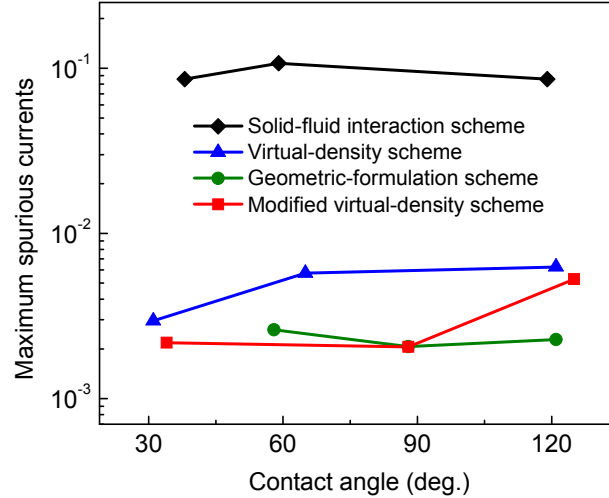
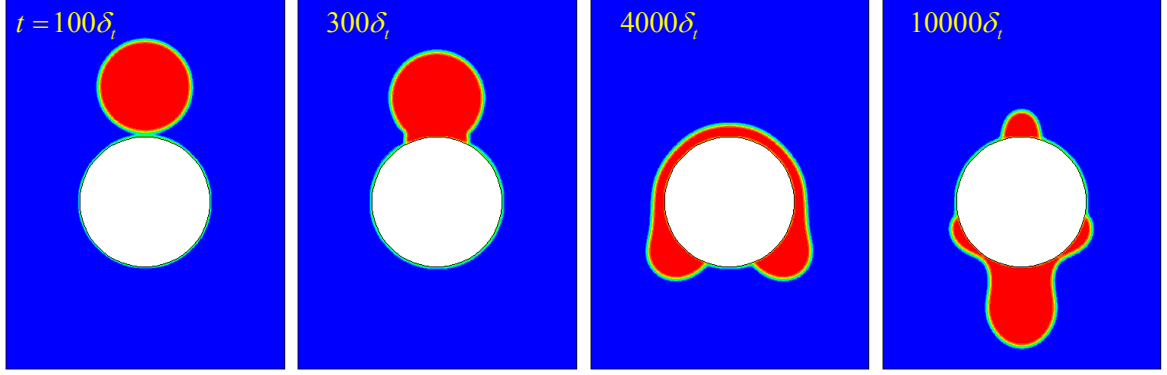
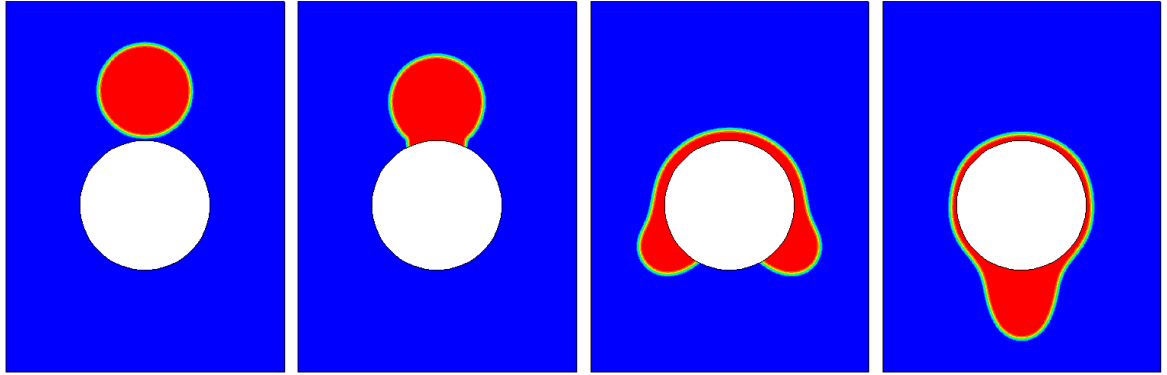


**FIG. 8.** Comparison of the maximum spurious currents caused by different contact angle schemes.

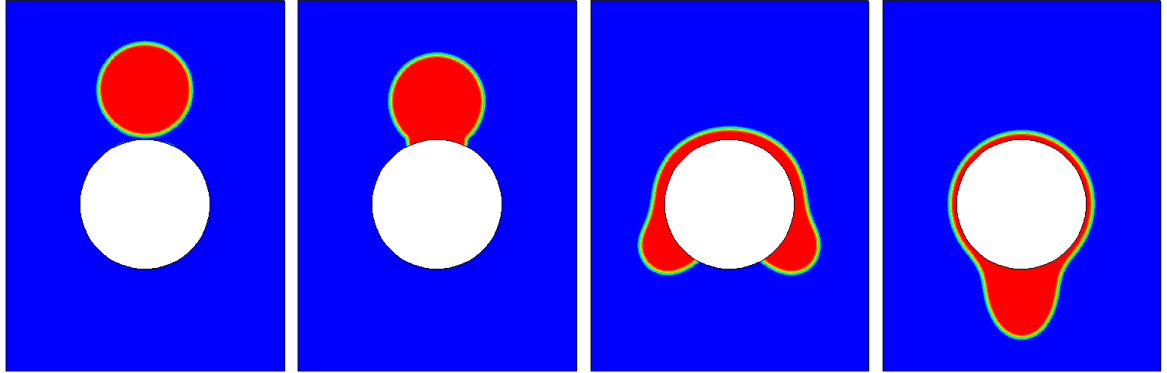
Some snapshots of the results obtained by the virtual-density scheme, the geometric-formulation scheme, and the modified virtual-density scheme are displayed in Figs. 9(a), 9(b), and 9(c), respectively. From Fig. 9(a) we can see that, when using the virtual-density scheme, the solid circular cylinder behaves like a droplet at the early stage due to an unphysical thick mass-transfer layer that encloses it. For example, at  $t = 100\delta_t$  the droplet has contacted the circular cylinder through the unphysical mass-transfer layer around the solid surface, while there is no such a phenomenon in the results of the geometric-formulation scheme and the modified virtual-density scheme. Owing to the influence of the unphysical mass-transfer layer, the numerical results predicted by the virtual-density scheme gradually deviate from the results obtained by the geometric-formulation scheme, which can be found by comparing Fig. 9(a) with Fig. 9(b). Particularly, significant deviations can be observed at  $t = 10000\delta_t$ . In contrast to the original virtual-density scheme, the modified virtual-density scheme is shown to be able to produce numerical results consistent with those given by the geometric-formulation scheme.



(a) virtual-density scheme



(b) geometric-formulation scheme



(c) modified virtual-density scheme

**FIG. 9.** Droplet impact on a cylindrical surface at  $Re = 600$  and  $\theta \approx 60^\circ$ . A comparison of the results obtained by (a) the virtual-density scheme, (b) the geometric-formulation scheme, and (c) the modified virtual-density scheme. From left to right:  $t = 100\delta_t$ ,  $300\delta_t$ ,  $4000\delta_t$ , and  $10000\delta_t$ .

Finally, the capability of the modified virtual-density scheme for simulating three-dimensional contact angles is validated by the test of static contact angles on a spherical surface. The D3Q19 pseudopotential MRT-LB model proposed in Ref. [33] is adopted in our simulations and the lattice system is chosen as  $N_x \times N_y \times N_z = 200 \times 200 \times 280$ . Initially, a solid sphere of radius  $R = 50$  is

located at  $(100, 100, 100)$  and a droplet of  $r = 45$  is placed on the spherical surface with its center at  $(100, 100, 180)$ . The periodic boundary condition is applied in all the directions and the halfway bounce-back scheme is employed to treat the solid boundary. The other treatments such as the equation of state and the coexisting densities of the two-phase system are the same as those used in the above two-dimensional tests. Figure 10 presents the results of different three-dimensional contact angles obtained by the modified virtual-density scheme, in which the lower row displays the density contours of the  $x$ - $z$  cross-section at  $y = 100$ . The results demonstrate that the modified virtual-density scheme is capable of modeling three-dimensional contact angles on a curved surface and does not suffer from a thick mass-transfer layer near the solid boundary, which exists in the simulations using the original virtual-density scheme.

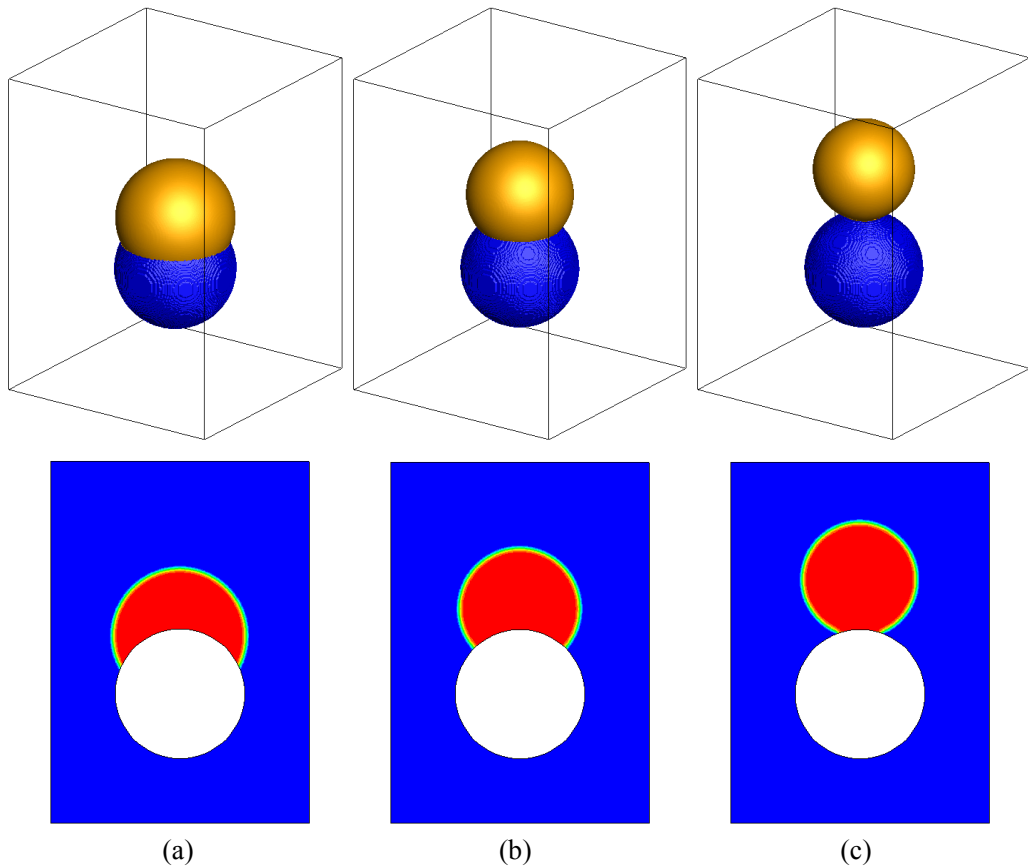


**FIG. 10.** Validation of the modified virtual-density scheme for simulating 3D contact angles on a curved surface. A 3D view is shown in the upper row, while in the lower row the density contours of the  $x$ - $z$  cross-section at  $y = 100$  are presented. (a)  $\varphi = 1.2$  with  $\theta \approx 53^\circ$ , (b)  $\varphi = 1$  with  $\theta \approx 88^\circ$ , and (c)  $\Delta\rho = 0.55$  with  $\theta \approx 145^\circ$ .

## V. Summary

We have investigated the implementation of contact angles in the pseudopotential LB simulations involving curved boundaries. The solid-fluid interaction scheme and the virtual-density scheme, which are two popular schemes for the pseudopotential LB modeling of wetting phenomena, are shown to suffer from very large spurious currents and an unphysical thick mass-transfer layer near the solid boundary, respectively. A curved geometric-formulation scheme for the pseudopotential LB model has been extended from a recently developed contact angle scheme for two-dimensional phase-field simulations. Although the geometric-formulation scheme can give a slope of the liquid-gas interface that is basically consistent with the prescribed contact angle, it is rather difficult to implement and cannot be directly applied to three-dimensional space. Hence we have proposed a modified virtual-density scheme, which employs a local virtual density to replace the constant virtual density and therefore overcomes the drawback of the original virtual-density scheme. Meanwhile, the spurious currents produced by the modified virtual-density scheme are much smaller than those caused by the solid-fluid interaction scheme and it is much easier to implement in both two-dimensional and three-dimensional space as compared with the geometric-formulation scheme. The features of the modified virtual-density scheme have been numerically demonstrated by simulating contact angles on cylindrical and spherical surfaces.

## Acknowledgments

This work was supported by the National Natural Science Foundation of China (No. 51822606).

## References

- [1] S. Chen and G. D. Doolen, *Annual Review of Fluid Mechanics* **30**, 329 (1998).
- [2] C. K. Aidun and J. R. Clausen, *Annual Review of Fluid Mechanics* **42**, 439 (2010).
- [3] Q. Li, K. H. Luo, Q. J. Kang, Y. L. He, Q. Chen, and Q. Liu, *Progress in Energy and Combustion Science*

52, 62 (2016).

[4] A. Xu, W. Shyy, and T. Zhao, *Acta Mechanica Sinica* **33**, 555 (2017).

[5] S. Succi, *Europhysics Letters* **109**, 50001 (2015).

[6] Z. Guo and C. Shu, *Lattice Boltzmann Method and Its Applications in Engineering* (World Scientific, 2013).

[7] H. Huang, M. Sukop, and X. Lu, *Multiphase lattice Boltzmann methods: Theory and application* (John Wiley & Sons, 2015).

[8] T. Krüger, H. Kusumaatmaja, A. Kuzmin, O. Shardt, G. Silva, and E. M. Viggen, *The Lattice Boltzmann Method - Principles and Practice* (Springer Nature, 2017).

[9] X. Shan and H. Chen, *Phys. Rev. E* **47**, 1815 (1993).

[10] X. Shan and H. Chen, *Phys. Rev. E* **49**, 2941 (1994).

[11] X. Shan, *Phys. Rev. E* **77**, 066702 (2008).

[12] N. S. Martys and H. Chen, *Phys. Rev. E* **53**, 743 (1996).

[13] P. Raiskinmäki, A. Koponen, J. Merikoski, and J. Timonen, *Computational Materials Science* **18**, 7 (2000).

[14] P. Raiskinmäki, A. Shakib-Manesh, A. Jäsberg, A. Koponen, J. Merikoski, and J. Timonen, *Journal of Statistical Physics* **107**, 143 (2002).

[15] Q. Kang, D. Zhang, and S. Chen, *Phys. Fluids* **14**, 3203 (2002).

[16] Q. Kang, D. Zhang, and S. Chen, *Journal of Fluid Mechanics* **545**, 41 (2005).

[17] C. E. Colosqui, M. E. Kavousanakis, A. G. Papathanasiou, and I. G. Kevrekidis, *Phys. Rev. E* **87**, 013302 (2013).

[18] R. Benzi, L. Biferale, M. Sbragaglia, S. Succi, and F. Toschi, *Phys. Rev. E* **74**, 021509 (2006).

[19] M. Latva-Kokko and D. H. Rothman, *Phys. Rev. E* **72**, 046701 (2005).

[20] T. Akai, B. Bijeljic, and M. J. Blunt, *Advances in Water Resources* **116**, 56 (2018).

[21] H. Huang, Z. Li, S. Liu, and X.-y. Lu, *International Journal for Numerical Methods in Fluids* **61**, 341 (2009).

[22] H. Huang, D. T. Thorne, M. G. Schaap, and M. C. Sukop, *Phys. Rev. E* **76**, 066701 (2007).

[23] H. Ding and P. D. M. Spelt, *Phys. Rev. E* **75**, 046708 (2007).

[24] Q. Li, P. Zhou, and H. J. Yan, *Langmuir* **32**, 9389 (2016).

[25] Y. Yu, Q. Li, C. Q. Zhou, P. Zhou, and H. J. Yan, *Applied Thermal Engineering* **127**, 1346 (2017).

[26] H.-R. Liu and H. Ding, *Journal of Computational Physics* **294**, 484 (2015).

[27] K. N. Premnath and J. Abraham, *Journal of Computational Physics* **224**, 539 (2007).

[28] Q. Li, K. H. Luo, and X. J. Li, *Phys. Rev. E* **87**, 053301 (2013).

[29] D. d'Humières, I. Ginzburg, M. Krafczyk, P. Lallemand, and L. S. Luo, *Philosophical Transactions of the Royal Society of London, Series A* **360**, 437 (2002).

[30] M. E. McCracken and J. Abraham, *Phys. Rev. E* **71**, 036701 (2005).

[31] L.-S. Luo, W. Liao, X. Chen, Y. Peng, and W. Zhang, *Phys. Rev. E* **83**, 056710 (2011).

[32] A. Xu, T. S. Zhao, L. An, and L. Shi, *International Journal of Heat and Fluid Flow* **56**, 261 (2015).

[33] Q. Li, D. H. Du, L. L. Fei, and K. H. Luo, *Computers & Fluids* **186**, 128 (2019).

[34] P. Yuan and L. Schaefer, *Phys. Fluids* **18**, 042101 (2006).

[35] H. Huang, M. Krafczyk, and X. Lu, *Phys. Rev. E* **84**, 046710 (2011).

[36] Q. Li, K. H. Luo, and X. J. Li, *Phys. Rev. E* **86**, 016709 (2012).

[37] M. Sbragaglia, R. Benzi, L. Biferale, S. Succi, K. Sugiyama, and F. Toschi, *Phys. Rev. E* **75**, 026702 (2007).

[38] D. Zhang, K. Papadikis, and S. Gu, *International Journal of Multiphase Flow* **64**, 11 (2014).

[39] Q. Li, K. H. Luo, Q. J. Kang, and Q. Chen, *Phys. Rev. E* **90**, 053301 (2014).

[40] Z. Xu, H. Liu, and A. J. Valocchi, *Water Resources Research* **53** (2017).

[41] Q. Li, Q. J. Kang, M. M. Francois, Y. L. He, and K. H. Luo, *Int. J. Heat Mass Transf.* **85**, 787 (2015).